Human Brain Mapping

WILEY

TECHNICAL REPORT OPEN ACCESS

Rosette Spectroscopic Imaging for Whole-Brain Slab Metabolite Mapping at 7T: Acceleration Potential and Reproducibility

Zhiwei Huang[1,2] | Uzay Emir[3,4,5] | André Döring[1,2] | Antoine Klauser[6] | Ying Xiao[1,2,7] | Mark Widmaier[1,2,7] | Lijing Xin[1,2,7]

[1]CIBM Center for Biomedical Imaging, Lausanne, Switzerland | [2]Animal Imaging and Technology, Ecole Polytechnique Fédérale de Lausanne (EPFL), Lausanne, Switzerland | [3]Department of Radiology, University of North Carolina at Chapell Hill, Chapell Hill, North Carolina, USA | [4]Biomedical Research Imaging Center (BRIC), University of North Carolina at Chapell Hill, Chapell Hill, North Carolina, USA | [5]Joint Department of Biomedical Engineering, University of North Carolina at Chapell Hill, Chapell Hill, North Carolina, USA | [6]Advanced Clinical Imaging Technology, Siemens Healthineers International AG, Lausanne, Switzerland | [7]Institute of Physics (IPHYS), Ecole Polytechnique Fédérale de Lausanne (EPFL), Lausanne, Switzerland

Correspondence: Lijing Xin (lijing.xin@epfl.ch)

Received: 9 October 2024 | **Revised:** 25 January 2025 | **Accepted:** 12 February 2025

Funding: This work was supported by Swiss National Science Foundation, 189064, 213769.

Keywords: ^{1}H magnetic resonance spectroscopic imaging | 7T | compressed sensing | reproducibility | rosette trajectory

ABSTRACT

Whole-brain proton magnetic resonance spectroscopic imaging (^{1}H-MRSI) is a non-invasive technique for assessing neurochemical distribution in the brain, offering valuable insights into brain functions and neural diseases. It greatly benefits from the improved SNR at ultrahigh field strengths (≥ 7T). However, ^{1}H-MRSI still faces several challenges, such as long acquisition time and severe signal contamination from water and lipids. In this study, 2D and 3D short TR/TE ^{1}H-FID-MRSI sequences using rosette trajectories were developed with nominal spatial resolutions of $4.48 \times 4.48\,mm^2$ and $4.48 \times 4.48 \times 4.50\,mm^3$, respectively. Water signals were suppressed using an optimized Five-variable-Angle-gaussian-pulses-with-ShorT-total-duration (FAST) water suppression scheme of 76 ms, and lipid signals were removed using the L_2 regularization method. Metabolic maps of major ^{1}H metabolites were obtained in 5:40 min with 16 averages and 1 average for the 2D and 3D acquisitions, respectively. Excellent intra-session reproducibility was shown, with the coefficients of variance (CV) being lower than 6% for N-Acetyl-L-aspartic acid (NAA), Glutamate (Glu), total Choline (tCho), Creatine and Phosphocreatine (tCr), and Glycine and Myo-inositol (Gly + Ins). To explore the potential of further acceleration, compressed sensing was applied retrospectively to the 3D datasets. The structural similarity index (SSIM) remained above 0.85 and 0.8 until $R = 2$ and 3 for the metabolite maps of Glu, NAA, tCr, and tCho, indicating the possibility for further reduction of acquisition time to around 2 min.

1 | Introduction

Proton magnetic resonance spectroscopic imaging (^{1}H MRSI) is a non-invasive technique to assess the spatial distribution of metabolites in the human brain. The free induction decay (FID) MRSI sequence is the most popular among different sequences due to its high signal-to-noise ratio (SNR) using ultra-short acquisition delay (TE) and short TR (Bogner et al. 2012, 2021; Klauser et al. 2021; Nassirpour, Chang, and Henning 2018). However, the long acquisition time of the conventional phase encoding scheme still limits its application in clinical settings.

Higher accelerations can be achieved with spatial-spectral encoding (SSE) techniques (Bogner et al. 2021). By sampling

Summary

- 2D-/3D- whole-brain slab non-lipid-suppression ultra-short-TE ^{1}H-MRSI acquisition schemes were implemented using the rosette trajectory with an optimized water suppression scheme and an adaptive voxel-wise L_2 lipid removal method.
- The method showed excellent intra-session reproducibility, with the coefficients of variance of major metabolites, such as creatine (Cr), glutamate (Glu), N-Acetyle-L-aspartic acid (NAA), and so on, below 5%.
- By retrospectively applying compressed sensing, the 3D acquisition time can potentially be reduced to about 2 min.

spatial and spectral information simultaneously utilizing high-slew-rate gradient waveforms, SSE techniques allow 25–170 times faster MRSI scans than conventional phase-encoding MRSI (Gagoski 2011). Common SSE techniques exploit trajectories (Bogner et al. 2021) like spiral (Hiba et al. 2003), rosette (Schirda et al. 2009), concentric rings (Chiew et al. 2018; Hingerl et al. 2018; Steel et al. 2018), and echo-planar trajectories (Mulkern and Panych 2001).

Several approaches have been proposed to further shorten the acquisition time. Parallel imaging techniques, such as SENSE, GRAPPA, and CAIPIRINHA (Breuer et al. 2006; Griswold et al. 2002; Pruessmann et al. 1999), leveraging the surplus of spatial information provided by multi-channel coil arrays, can help accelerate data collection during the acquisition stage; but the acceleration rate is limited by noise amplification due to the reduced number of phase encoding lines and the geometric factor (Deshmane et al. 2012). Compressed sensing (CS) with random undersampling patterns, leveraging the intrinsic sparsity of the signal, can surpass the Nyquist sampling criteria, enabling acceleration rates of up to 3–5 for MRSI in the brain (Klauser et al. 2023; Nassirpour, Chang, Avdievitch, and Henning 2018).

Ultra-high field strengths offer additional benefits, including higher SNR and improved spectral resolution, which can enhance metabolite detection and quantification. However, they also require broader spectral bandwidths, posing challenges due to the restriction in maximum gradient amplitudes and slew rates. One solution to alleviate the restriction is to use temporal interleaves, but it will increase the acquisition time and potentially introduce other artifacts (Bogner et al. 2021). Among different k-space sampling trajectories, the rosette trajectory exhibits higher flexibility and poses less demand on the gradients. Besides, the rosette trajectory oversamples the k-space center and can improve the temporal SNR (Bucholz et al. 2008). Also, that the rosette trajectory goes across the k-space center in each repetition allows for self-correction techniques of frequency drift and motion artifacts without leveraging navigators (Senthil et al. 2023), making it more robust to systematic frequency drift and motion artifacts. Moreover, the trajectory was designed based on the stochastic trajectory (Noll 1997), which is intrinsically incoherent, making it more compatible with CS for further acceleration.

The inhomogeneous B_1^+ distribution at high magnetic fields poses another challenge. It can deteriorate the overall water suppression efficiency, leading to high water residuals and substantial water sidebands. The water sideband can overlap with metabolite signals depending on the applied gradients, spectral bandwidths (Ozdemir et al. 2006), and residual water amplitudes, making spectral fitting and metabolite quantification challenging. The established WET water suppression scheme (Water suppression Enhanced through T_1 effects) (Ogg et al. 1994) is widely used in MRS and MRSI sequences (Tkáč et al. 2021) given its total duration and SAR level. However, it suffers from reduced global water suppression efficiency at 7T and above. With the incorporation of ultra-short TE and non-Cartesian trajectories which necessitate stronger gradients, the sideband problem gets worse (Serrai et al. 2002). Several studies optimized the water suppression scheme based on the WET scheme (Hangel et al. 2018; Klauser et al. 2023; Mahmud et al. 2023), but no study has shown the performance before and after the optimization.

Until now, rosette spectroscopic imaging (RSI) is mostly demonstrated at 3T, where the trajectory parameters were optimized for temporal SNR (Schirda et al. 2009). However, when it comes to the whole-brain RSI at 7T, few studies have been reported. Schirda C. et al. developed RSI at 7T with LASER pre-localization and outer volume suppression (OVS) of the skull lipid signal, exciting the inner part of the brain (Schirda et al. 2016). Whole-brain slab MRSI including the measurements in the cortical regions, often does not apply OVS and relies on lipid removal strategies such as the L_2 regularized lipid removal (Bilgic et al. 2014), data extrapolation (Haupt et al. 1996), FLIP (Adany et al. 2021) etc. Mahmud et al. reported a 2D whole-brain slice ^{1}H-FID RSI at 7T, achieving a 2 mm nominal in-plane resolution using three temporal interleaves, with an acquisition time of approximately 6 min (Mahmud et al. 2023). Recently, a modified egg-shaped rosette trajectory with two temporal interleaves was proposed. It allows 2D measurements with 3.44 mm in-plane resolution and a scan time of 6:04 min, as well as 3D measurements with a resolution of $3.44 \times 3.44 \times 4.47\,mm^3$ and a scan time of 19 min (Blömer et al. 2024).

This study seeks to advance the ^{1}H RSI at 7T by improving global water suppression performance, shortening TE, evaluating the reproducibility of the estimated metabolite maps, lipid removal performance, and further reducing the acquisition time with CS for whole brain metabolites mapping.

2 | Materials and Methods

The sequence diagrams are shown in Figure 1a. An asymmetric amplitude-modulated RF pulse (P10) with a duration of 2048 μs and a bandwidth of 2700 Hz (center frequency at 4.7 ppm for the water scan, 2.4 ppm for the metabolite scan) was used for excitation to enable an ultra-short acquisition delay (TE) of sub-milliseconds.

2.1 | Trajectory Design

The rosette trajectory can be described by a rapid sinusoidal oscillation rotating in the $k_x - k_y$ plane (Noll 1997) (1), where $k_{max} = \frac{N_x}{2FOV}$.

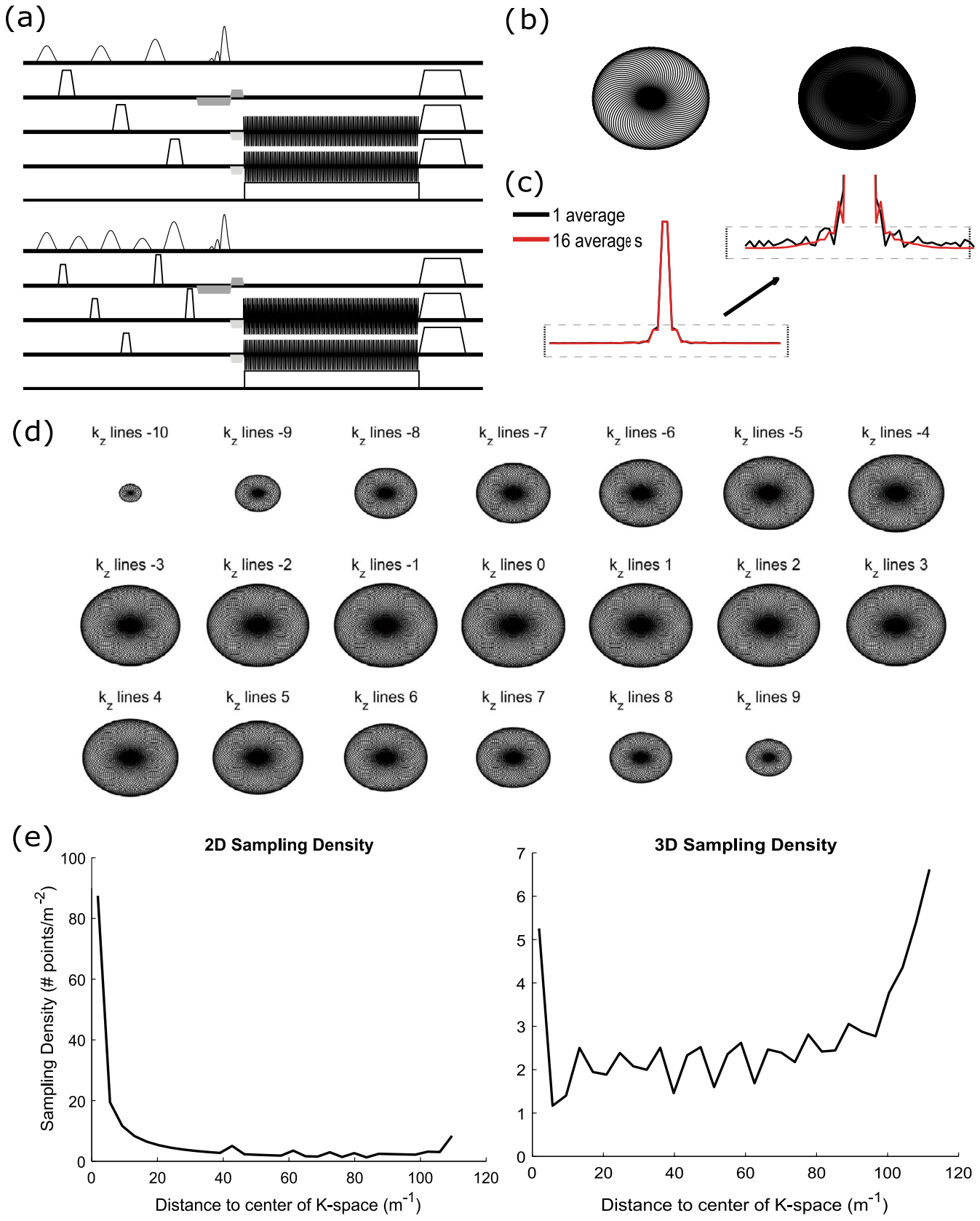

FIGURE 1 | (a) The sequence diagrams with the WET (top) and the FAST (bottom) water suppression scheme; dark gray: Localization and corresponding rewinding gradients; light gray: Rewinding gradients for the trajectory; blank with black outline: Spoiler gradients; (b) The 2D rosette trajectory with 79 petals (left, NA = 1) and 100 petals (right, NA~1.27); half petals were shown for the sake of visualization, (c) Comparison of normalized SRF of rotating average and simple average with NA = 16; (d) The 3D trajectory with a stack of rosette trajectories with a spherical bound in the k-space. (e) The sampling density of the 2D and 3D trajectories.

$$k(t) = k_{max}\sin(\omega_1 t)e^{i\omega_2 t} \quad (1)$$

The selection of ω_1 and ω_2 is constrained by the maximum gradient amplitude, slew rate, and spectral bandwidth (2, 3, 4).

$$|G_x| \le \frac{2\pi}{\gamma} k_{max} \max(\omega_1, \omega_2) \quad (2)$$

$$|S| \le \frac{2\pi}{\gamma} k_{max}(\omega_1^2 + \omega_2^2) \quad (3)$$

$$\gamma FOV\, G_{max} + SBW \le \frac{1}{dt} \quad (4)$$

Here, $\omega_1 = \omega_2 = 2000\pi$ Hz was chosen to achieve the maximum spatial resolution with a spectral bandwidth of 2000 Hz to cover a ^{1}H spectral range of 6.7 ppm (1.34–8.06 ppm). The maximum gradient amplitude and slew rate were 16.46 mT/m and 206.96 mT/m/ms, respectively, restricted by the peripheral nerve stimulation (PNS) limits. The resulting in-plane resolution is $4.48 \times 4.48\,mm^2$. $N_{sh} = 79$ petals were acquired for a fully sampled 2D acquisition (Schirda et al. 2009).

To improve the spatial response function (SRF), a rotating averaging scheme was used. Instead of N_{sh} petals repeated by the number of average (NA), $NA \times N_{sh}$ petals were acquired (Figure 1b). The SRF for the normal averaging mode and rotating averaging mode are shown in Figure 1c. To extend the scheme to 3D k-space sampling, a stack of rosette trajectories in the $k_x - k_y$ plane was exploited, with the k_z direction being Cartesian phase encoded. A spherical bound in 3D was used (Figure 1d): the maximum k_{xy} and the number of petals N_{sh_z} in each k_z plane are given by (5, 6):

$$k_{xy_{max}} = \max\left(\sqrt{k_{max}^2 - k_z^2}, 0.2k_{max}\right) \quad (5)$$

$$N_{sh_z} = ceil\left(\frac{k_{xy_{max}}}{k_{max}} N_{sh_0}\right) \quad (6)$$

where N_{sh_0}, N_{sh_z} are the number of petals in the slices with k_z being 0 or z, k_{max} is the maximum k value in the $k_x - k_y$ plane in the central slice. The spatial resolution is $4.48 \times 4.48 \times 4.50\,mm^3$, with 20 slices covering 90 mm FOV along z-axis.

The k-space sampling density of the trajectories is shown in Figure 1e. The 2D trajectory samples most densely in the k-space center. The sampling density then goes down with k_r and goes up a bit in the outer k-space, being consistent with visual perception. The 3D rosette trajectory shows lower sampling density in the k-space center. This is due to the Cartesian phase encoding along the k_z direction, where the sampling density in each k_z plane follows the 2D trend, but most k_z planes do not go across the k-space center (0, 0, 0). Using a 3D rotating rosette trajectory can achieve denser sampling in the k-space center, however, it will take almost twice as long as the current setting to achieve the same resolution while fulfilling the Nyquist sampling criteria.

2.2 | Water Suppression Scheme

The established WET water suppression scheme (Ogg et al. 1994) consists of three Gaussian pulses with flip angles of 89.2°, 83.4°, 160.8°, and equal inter-pulse delays of 60 ms (total duration of 180 ms). The scheme was optimized to T_1 and B_1^+ insensitivity at 1.5 T. However, the B_1^+ inhomogeneity is more severe at higher field strength, which necessitates higher requirements for B_1^+ insensitivity. To improve the water suppression efficiency at 7T, we optimized the water suppression scheme tailoring for B_1^+ insensitivity. The new water suppression scheme consists of Five variable Angle gaussian pulses with a ShorT total duration of 76 ms (FAST). The flip angles are 100°, 80°, 125°, 65°, and 170°, optimized based on Bloch simulation by minimizing water magnetization along *z*-axis before excitation, aiming for B_1^+ insensitivity (7), where B_1^+ of 1 corresponds to the nominal flip angle:

$$\min_{flipAngle_{1,2,3,4,5}} \sum_{B_1 + \in [0.1, +1.5]} \left| \frac{M_{z,B1+}}{M_0} \right| \quad (7)$$

The inter-pulse delays are 15, 15, 15, 17, and 14 ms, respectively. These values were selected to achieve the shortest water suppression module duration while at the same time allow for flexibility in water suppression bandwidth (≥80 Hz) and crusher gradient moment selection. The crusher gradients were set based on the WET scheme but not optimized systematically. The current gradient moments are 168, 168, 168, 235, and 235 ms*mT/m, respectively. No spurious echoes were observed in the acquired spectra. The proposed FAST scheme is robust to [−50, +60] % variation in the B_1^+ field, achieving a 98% suppression efficiency (Figure 2a). Besides, the shorter duration of the water suppression block allows for reducing the minimum TR from 370 to 270 ms.

2.3 | Phantom and Participants

The sequence was tested on a spherical phantom (*Gold Standard Phantoms, spectre*, diameter of 18 cm) for validation, which contains seven metabolites at physiological pH and concentrations (12.5 mM N-Acetyle-L-aspartic acid (NAA), 10.0 mM Creatine (Cr), 3.0 mM Choline Chloride (Cho), 7.5 mM Myo-inositol (Ins), 12.5 mM Glutamate (Glu), 5.0 mM Lactate (Lac), and 2.0 mM GABA). Three healthy subjects (28–40 years old, 2 males and 1 female) were scanned for this study. All volunteers gave informed consent in accordance with the Swiss cantonal ethics committee before the experiments.

2.4 | MR Acquisition

All experiments were performed on a 7T MAGNETOM Terra X scanner (Siemens Healthineers, Forchheim, Germany), with an 8-channel transmit coil with 32 receiver arrays (Nova Medical Inc. Wilmington MA, USA). The maximum allowed gradient amplitude and slew rate are 130 mT/m and 250 mT/m/s, respectively. First-, second- and third-order B_0 shimming were implemented using the vendor-pre-implemented *DESS Advanced* scheme.

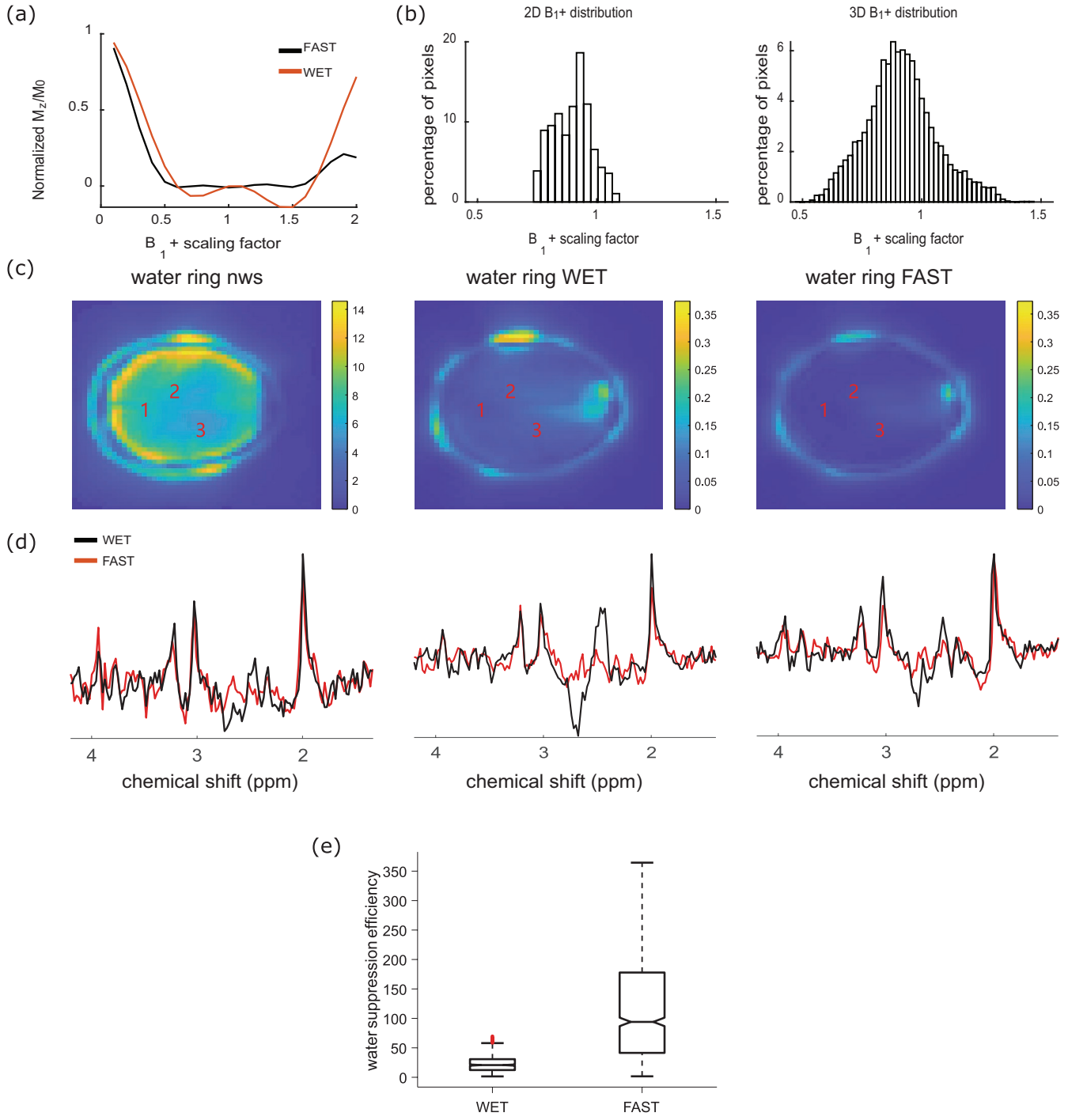

FIGURE 2 | (a) Simulated water suppression efficiency v.s B_1^+: $B_1^+ = 1$ corresponds to the nominal flip angle. (b) Measured 2D and 3D B_1^+ distribution in a representative subject using the Siemens product tfl_rfmap sequence with the same 2D or 3D field of view as in the RSI measurements. In the 3D case, the first three and last two slices of the B_1^+ map were excluded to align with the 3D RSI datasets. (c) Water maps (absolute spectral sum within the range [4.3, 5.1] ppm of the non-water-suppressed data, WET water-suppressed data, and FAST water-suppressed data; (d) Sample spectra of the WET and FAST water-suppressed data, from left to right are voxel 1–3. The WET spectra showed obvious sidebands, which were alleviated in the FAST spectra; (e) box plot of the voxel-wise water suppression efficiency of the WET and FAST water-suppressed data.

Phantom experiments: To validate the sequence, 2D RSI measurements were performed with an FOV of $224 \times 224\,mm^2$, a matrix size of 50×50, and TE/TR = 0.87/370 ms (NA = 1, total scan time 22 s). Considering that the in vitro linewidth is narrower than that in vivo, a 2 Hz exponential filter was applied in the temporal domain. Metabolite concentrations were quantified and corrected by their T_1 relaxation times (Table S1).

In vivo experiments: A T_1-weighted anatomical image was first acquired with the MP2RAGE sequence (TE/TR = 1.54 ms/5500 ms, TI_1/TI_2 = 750 ms/2350 ms, $\alpha_1/\alpha_2 = 4°/5°$,

FOV = 169 × 248 × 256 mm^3, matrix size = 256 × 404 × 416) (Marques et al. 2010). The 2D RSI data were acquired with a FOV of 224 × 224 mm^2, a matrix size of 50 × 50, and a slice thickness of 10 mm. The acquisition took 21.33 s per average. 16 averages were acquired to improve the SNR, leading to a total acquisition time of 5:41 min. An additional water scan (NA = 1, acquisition time (TA) = 22 s) was obtained for coil combination and metabolite quantification. The 3D RSI data was acquired with an FOV of 224 × 224 × 90 mm^3. An excitation slab of 65 mm was adopted to avoid aliasing artifacts. The matrix size was 50 × 50 × 20, leading to a nearly isotropic resolution of 4.50 mm. The total acquisition was 5:38 min for the metabolite data (TR = 270 ms), and 4:00 min for the water scan (TR = 190 ms). The TE for the 2D and 3D acquisitions were 0.87 ms and 0.83 ms, respectively. The flip angle (FA) was set to the Ernst angle assuming the average metabolite T_1 being 1800 ms (Klauser et al. 2021) (TR = 270 ms, FA = 31°; TR = 190 ms, FA = 26°). Both acquisitions were repeated twice without replacing the subjects to evaluate the intra-session reproducibility, with the delay between two acquisitions being 10 min. The 2D and 3D (the central 15 slices) B_1^+ maps were measured with the vendor sequence tfl_rfmap with the same FOV as the corresponding RSI acquisitions.

In addition, to compare the water suppression performance, 2D RSI with the WET scheme and the proposed FAST water suppression scheme was measured with the same FOV and matrix size (TE/TR = 0.87/370 ms, NA = 12, FA = 36°) in one volunteer.

2.5 | Reconstruction and Data Analysis

Reconstruction and post-processing: The reconstruction and data analysis were performed offline using MATLAB R2023b (MathWorks Inc. Natick, MA, USA) and LCModel (Provencher 2001). The RSI data were reconstructed using the NUFFT operator (Fessler and Sutton 2003), with a 2D-Hanning filter applied in the $k_x - k_y$ plane and a 1D Hanning filter applied along k_z dimension. An adaptive coil combination was used (Walsh et al. 2000).

After reconstruction and coil combination, residual water was then removed through HLSVD (Lin et al. 2019), and lipid signals were removed using L_2 regularization in the spectral domain (Bilgic et al. 2014). The lipid mask (Figure 3a) was selected as the 100 voxels with the highest lipid signal sum (LSS) (Equation 8) outside the brain per slice based on the water-suppressed MRSI data. The regularization parameter was selected in a voxel-wise manner (Figure 3b). For each voxel, the regularization parameter was selected by increasing the parameter with an increment of one within the range of [1, 1000] until the LSS converged (Equation 9). The convergence threshold was selected as 0.005.

$$LSS = \sum_{i \in [0.7,1.8]ppm} abs(S_i), \quad S: spectra \tag{8}$$

$$\frac{LSS(reg_{i+1}) - LSS(reg_i)}{LSS(reg_i)} \leq threshold \tag{9}$$

Then, the regularization parameters in the peripheral voxels (4 layers of adjacent voxels to the edge of the brain mask) were chosen to give an LSS comparable to the center voxels to avoid potential residual lipids (Equation 10).

$$LSS_{peripheral} \leqq mean(LSS_{center}) + std(LSS_{center}) \tag{10}$$

The processed spectra were first-order phase corrected and then quantified using LCModel (Provencher 2001) within the range 1.6–4.2 ppm using water data as an internal quantification reference. Metabolite basis sets were simulated in MATLAB using the density matrix formalism including spin evolution during the P10 excitation pulse. The chemical shifts and J-coupling constants were taken from (Govindaraju et al. 2000). The basis set contained 21 simulated metabolites, including alanine (Ala), ascorbate (Asc), aspartate (Asp), Cr, phosphocreatine (PCr), glucose (Glc), glutamine (Gln), Glu, glutathione (GSH), glycerophosphocholine (GPC), phosphocholine (PCho), Ins, Lac, NAA, N-acetylaspartylglutamate (NAAG), Phosphoryl ethanolamine (PE), Scylla-inositol (Scyllo), taurine (Tau), GABA, glycine (Gly), serine (Ser). Altogether 14 brain metabolites were quantified. A CRLB threshold of 50% was used. The basis set also includes eight simulated macromolecule (MM) resonances generated by LCModel, including MM09, MM12, MM14, MM17, and MM20 at the following positions: 0.91, 1.21, 1.43, 1.67, 1.95, 2.08, 2.25, and 3 ppm. T_1 relaxation correction and water content correction were implemented (Bluestein et al. 2012; Xin et al. 2013). No T_2 relaxation correction was applied due to the use of ultra-short TE. To evaluate the spectral quality, water linewidth was estimated by Voigt line fitting using the water data, and SNR was calculated according to (Equation 11), where S_{NAA} and S_{noise} are the spectral signal within [1.85, 2.15] ppm and [5.1, 6.1] ppm. The water suppression efficiency was evaluated according to (Equation 12), where S_{ws} and S_{nws} are the water-suppressed and non-water-suppressed spectral signals within range [4.3, 5.1] ppm.

$$SNR = \frac{\max(real(S_{NAA}))}{std(real(S_{noise}))} \tag{11}$$

$$Water\ Suppression\ Efficiency = \frac{\sum abs(S_{nws})}{\sum abs(S_{ws})} \tag{12}$$

The anatomical images were segmented into gray matter (GM), white matter (WM), and cerebrospinal fluid (CSF) using FSL software (Jenkinson et al. 2012). Nine anatomical structural regions (caudate, cerebellum, frontal lobe, insula, occipital lobe, parietal lobe, putamen, temporal lobe, thalamus) were extracted according to a standard atlas (MNI structural atlas) (Collins et al. 1995; Mazziotta et al. 2001). Metabolite concentrations were analyzed in different tissue types and major brain lobes, and the intra-session reproducibility was evaluated using coefficients of variation (CV%).

2.6 | Compressed Sensing Optimization

For the sake of computational efficiency, the BART package (Uecker et al. 2013) was used for CS with the default ESPIRit coil combination method (Uecker et al. 2014). The CS reconstruction can be formulated as an optimization problem to reconstruct the

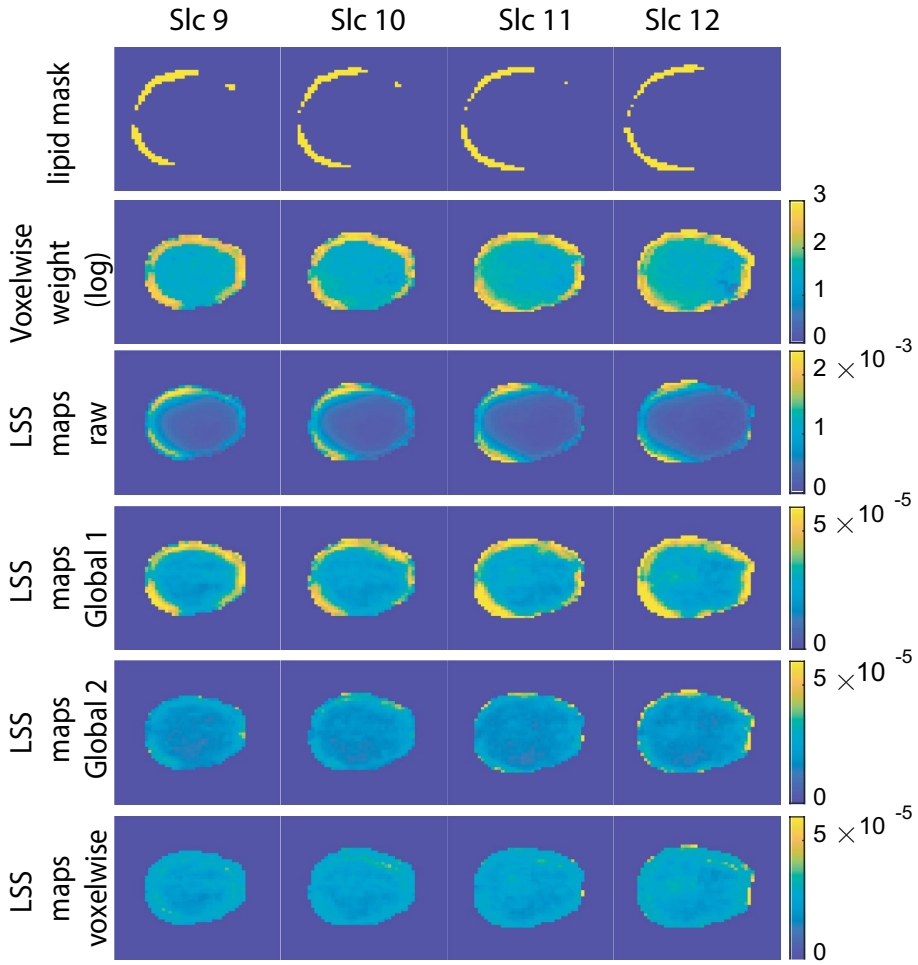

FIGURE 3 | The adaptive voxelwise L_2 lipid removal implementation, row: (1) sample lipid masks; (2) the adaptive voxelwise regularization parameters in log scale; (3–6) the lipid signal sum (LSS) map of the raw spectra, spectra after standard L_2 lipid removal using global regularization parameter 1 (28 here; for other 2D/3D datasets, the values vary from 10 to 30) and 2 (350 here; for other 2D/3D datasets, the values vary from 150 to 350) selected manually from a subset of central voxels and peripheral voxels based on spectra quality, and spectra after the adaptive L_2 lipid removal method.

data from undersampled measurements leveraging the intrinsic sparsity of the reconstructed signals. Total variation (TV) regularization was applied to the three spatial dimensions in the 3D datasets (Equation 13), where Fu is the non-uniform Fourier transform operator, x and y are the reconstructed signal and the measured signal. λ_1 is the hyper-parameter balancing between the data fidelity term and the sparsity constraint. The alternating direction method of multipliers (ADMM) optimizer (Wei and Ozdaglar 2012) was used to solve the optimization problem.

$$\min_x ||F_u x - y||_2 + \lambda_1 ||TV(x)||_1 \tag{13}$$

To explore the influence of undersampling patterns, retrospectively regular (every one of R petals sampled) and random (a random subset of petals sampled with the number of petals comparable to the regular undersampling) undersampling schemes were implemented at an acceleration rate (R) of 2. The performance was evaluated using the structural similarity index (SSIM) (Equation 14) between the fully sampled data (R1) and undersampled data (R2) in terms of the resulting metabolic maps (Glu, NAA, PCr + Cr (tCr), Cho + GPC (tCho)), where L is the dynamic range of the image, μ_x and μ_y are the mean value of the images, $\sigma_{xy}, \sigma_x, \sigma_y$ are the covariance and variance of the images.

$$\mathrm{SSIM(x,y)} = \frac{\left(2\mu_x\mu_y + 10^{-4}L^2\right)\left(2\sigma_{xy} + 9*10^{-4}L^2\right)}{\left(\mu_x^2 + \mu_y^2 + 10^{-4}L^2\right)\left(\sigma_x^2 + \sigma_y^2 + 9*10^{-4}L^2\right)} \tag{14}$$

The incoherence of the trajectories was evaluated using the maximum sidelobe-to-peak ratio (MSPR) (Equation 15) and the average sidelobe-to-peak ratio (ASPR) (Equation 16) (Lustig et al. 2007).

$$MSPR = \max_{i \neq j}\left[\frac{PSF_{i,j}}{PSF_{i,i}}\right] \tag{15}$$

$$ASPR = \underset{i \neq j}{average}\left[\frac{PSF_{i,j}}{PSF_{i,i}}\right] \tag{16}$$

The regular undersampling scheme was adopted for $R = 1$–6. The optimal hyper-parameter λ_1 was selected by iterating over a range of values between 10^{-4} and 1. The SSIM between the fully

sampled data (R1) and undersampled data (R2 to R6) were assessed for water images and metabolic maps (Glu, NAA, PCr + Cr (tCr), Cho + GPC (tCho)) to select the optimal parameter.

Only metabolite acquisitions were undersampled, considering that the water acquisition was needed for coil sensitivity map generation and could be shortened by reducing the number of spectral points in practice. The hyperparameter was optimized on one dataset and then applied to all other datasets.

3 | Results

3.1 | FAST Water Suppression Efficiency

Figure 2a shows the simulated water suppression efficiency of the WET and FAST schemes across different B_1^+. The FAST water suppression scheme showed substantial improvements (Figure 2c) in the range of [−50, +60] % variation in the B_1^+, which was sufficient to cover B_1^+ variances at 7T for 2D and 3D measurements (Figure 2b). The water sidebands in the spectra were alleviated (Figure 2d) in comparison to WET. The three quartiles of the water suppression efficiency of the WET scheme and the FAST scheme were 12.3, 20.7, 30.8 and 41.3, 94.0, 177.9, respectively.

3.2 | In Vivo Validation

Figure 4 presents 2D metabolic maps and the linewidth map. The metabolites successfully quantified over 85% of the voxels within the brain are shown (except for NAAG). The metabolic maps indicate anatomical features of GM and WM for each of the metabolites. Glu, tCr have higher concentrations in the GM, tCho, Gly + Ins, and NAAG are higher in WM. The average concentrations and the third quartile CRLBs for each metabolite in WM and GM are shown in Table 1, as well as the water linewidths and SNR.

Figure 5 presented 3D T_1 weighted anatomical images, metabolic maps, and water linewidth maps. The exclusion criteria were the same as that for the 2D data. The first three slices and the last two slices were discarded due to the aliasing artifacts and the RF pulse profile, leading to altogether 15 slices. The metabolic concentrations and third-quartile CRLBs, as well as the spectral quality metrics (SNR and water linewidth) are summarized in Table 1. It was observed that the central slices had better spectral quality than the peripheral slices, which was in line with the water linewidth distribution. The same GM/WM distributions were observed as that in the 2D datasets.

3.3 | Reproducibility Evaluation

CVs were calculated in the GM, WM, and several brain lobes, shown in Table 2. For 2D acquisitions, the mean CVs of NAA, tCho, tCr, Gly + Ins, and Glu were below 6% in the GM, WM, frontal lobe, and parietal lobe; the mean CVs of NAAG, GSH, and Tau were below 10%. For 3D acquisitions, the mean CVs of NAA, tCho, tCr, Gly + Ins, and Glu were below 5%, and those of NAAG, GSH, and Tau were mostly below 10% in GM, WM, frontal lobe, parietal lobe, temporal lobe, and occipital lobe. 3D data tend to show lower CVs than 2D data in the frontal lobe and parietal lobe.

3.4 | Retrospective Compressed Sensing Acceleration

The regularly undersampled (R2 odd, R2 even) and randomly undersampled (R2 rand1, R2 rand2) trajectories at $R = 2$ were

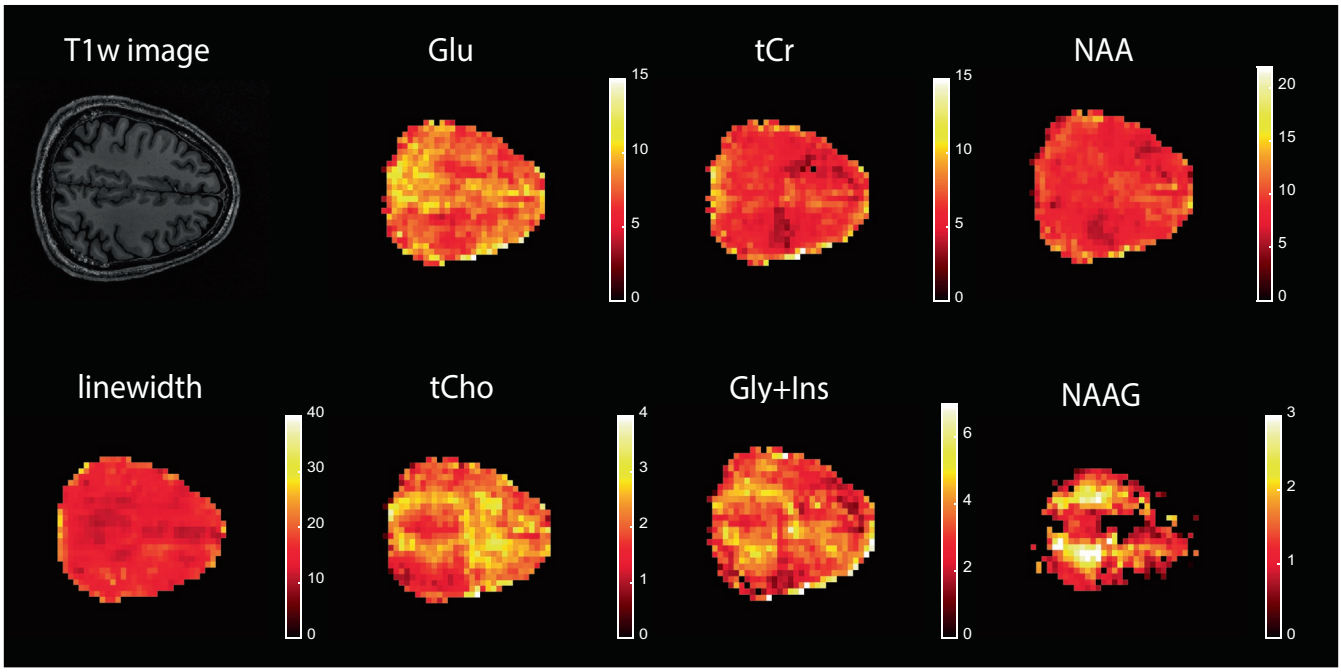

FIGURE 4 | 2D T_1-w image, the water linewidth map, and ^{1}H-FID RSI metabolic maps (i.u) of brain metabolites with CRLB lower than 50% in over 85% of the brain voxels and NAAG from a representative subject.

TABLE 1 | Metabolite concentrations (i.u), third-quartile CRLBs, linewidths, and spectral SNR (mean ± std).

		Glu	NAA	NAAG	tCho	tCr	Gly + Ins	LW	SNR
2D	GM (conc.)	7.98 ± 0.93	9.06 ± 0.50	1.02 ± 0.11	1.49 ± 0.41	6.38 ± 0.32	2.96 ± 0.23	14.45 ± 0.50	14.20 ± 0.48
	CRLB (%)	9.67 ± 2.08	7.00 ± 1.00	38.17 ± 2.75	14.67 ± 4.93	8.33 ± 0.58	19.00 ± 1.73		
	WM (conc.)	7.51 ± 1.15	9.11 ± 0.78	1.52 ± 0.33	1.81 ± 0.56	6.36 ± 0.42	3.42 ± 0.30	13.74 ± 0.25	14.69 ± 0.42
	CRLB (%)	12.25 ± 4.02	8.33 ± 1.15	31.33 ± 3.79	12.00 ± 4.36	9.00 ± 1.00	17.00 ± 1.00		
3D	GM (conc.)	7.42 ± 0.75	8.97 ± 0.71	1.31 ± 0.20	1.62 ± 0.27	6.55 ± 0.38	3.27 ± 0.57	21.67 ± 1.28	11.82 ± 2.11
	CRLB (%)	11.67 ± 2.52	8.00 ± 1.73	35.75 ± 0.43	12.67 ± 1.15	8.67 ± 0.58	18.67 ± 5.69		
	WM (conc.)	6.96 ± 0.62	8.96 ± 0.65	1.79 ± 0.36	1.98 ± 0.33	6.76 ± 0.43	3.68 ± 0.75	20.03 ± 1.19	12.35 ± 1.88
	CRLB (%)	14.67 ± 3.21	9.33 ± 2.31	30.67 ± 2.08	11.00 ± 1.00	9.33 ± 0.58	18.00 ± 5.29		

shown in Figure 6, as well as the resulting Glu, NAA, tCho, and tCr maps. It can be seen that in the metabolic maps generated from randomly sampled trajectories, there are more missing voxels compared to the regularly undersampled ones, as indicated by the CRLB values shown. Furthermore, metabolic maps of the regularly undersampled trajectories aligned better with the fully sampled ones, as indicated by SSIM values. These observations were coherent with the incoherence metrics (Table 3), where lower values indicated higher incoherence. Thus, regular undersampling was implemented for subsequent experiments.

The optimization process showed that $\lambda_1 = 0.05$ gave the highest SSIM in terms of the water images and metabolic maps concerning the fully sampled data. Thus, $\lambda_1 = 0.05$ was used for all datasets and acceleration rates.

Figure 7 shows the accelerated 3D metabolic maps with acceleration rates (R) of 1–6 from the central four slices. Figure 8 shows the corresponding spectra from 6 different voxels. It is shown that for Glu, the GM/WM contrast was preserved until $R = 3$. The mean concentrations, CRLBs, SSIM, and spectral SNR for different acceleration rates were shown in Table 4. Spectral SNR and SSIM decreased as R increased, with an average SSIM larger than 0.8 until $R = 3$.

4 | Discussion

In this study, we developed a 2D and 3D whole-brain slab non-lipid-suppression ultra-short TE MRSI acquisition scheme using the rosette trajectory. The method showed excellent intra-session reproducibility with an optimized water suppression scheme and processing pipeline. Additionally, it was shown that with CS, the 3D acquisition could be further shortened to around 2 min.

Residual water and lipid signals are two main sources of spectral contaminations for ^{1}H MRSI. The sidebands of the water resonance can fall inside the metabolite range and can overlap with some key metabolites such as Glu, causing bias or even failure in metabolite quantification. With the FAST water suppression scheme, the water suppression efficiency increased across a wide range of B_1^+, alleviating water sidebands and improving spectral quality. The short total duration of the FAST scheme enables the use of a short TR, further reducing the overall scanning time. Additionally, since only gaussian pulses were exploited in the scheme, the SAR was far from the limit. The predicted SAR values reported by the scanner for the WET and FAST schemes were around 0.6%, 0.9% and 4.9%, 7.2% for the whole body and head respectively with a normal volunteer weighing around 60 kg. Noteworthily, under the current crusher gradient scheme, no spurious echo was observed. Nevertheless, the crusher scheme can be further optimized if necessary (Landheer and Juchem 2019).

Lipids, another high-intensity signal from the skull, can contaminate the spectra due to signal propagation through the point spread function and the imperfection of the excitation pulse profile. Inversion recovery (IR) and OVS are two common methods of lipid suppression. However, additional pulses can increase RF energy deposition, leading to longer

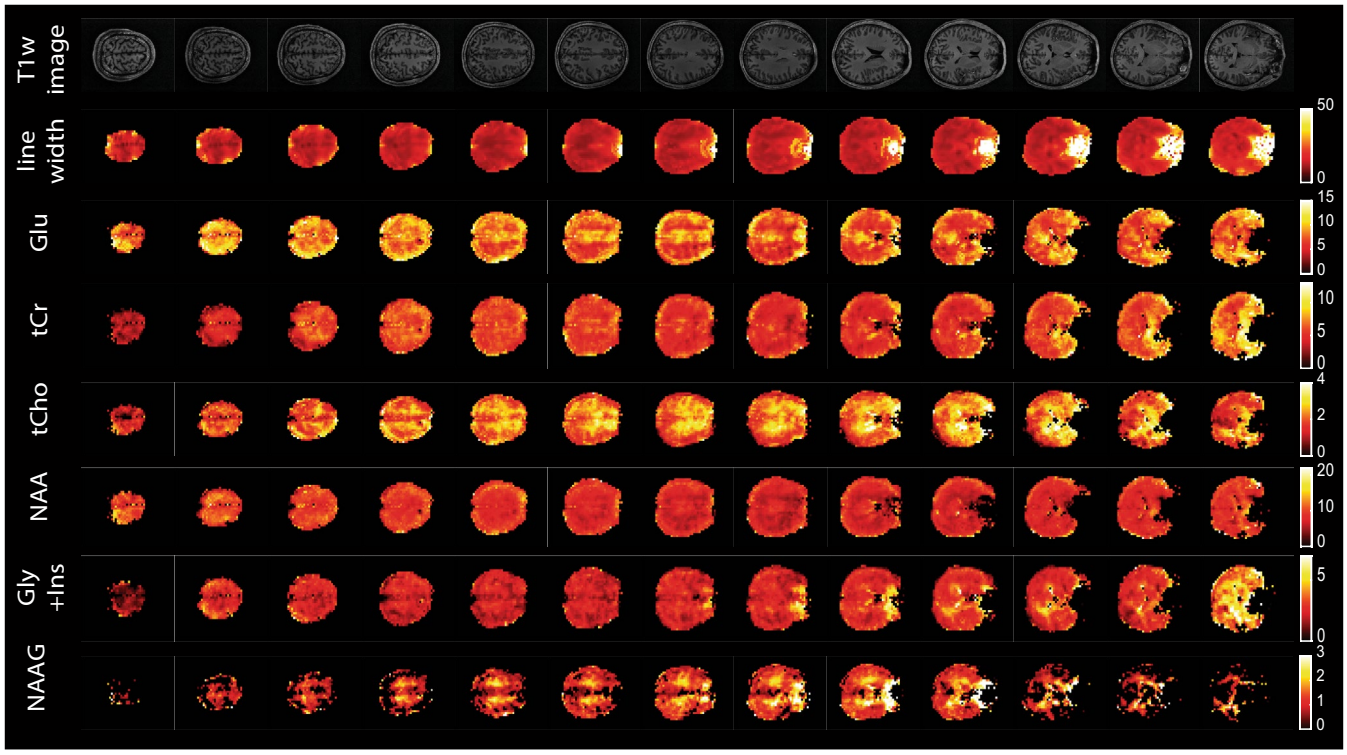

FIGURE 5 | 3D T_1-w images, water linewidth maps, and ^{1}H-FID RSI metabolic maps (i.u) of brain metabolites with CRLB lower than 50% in over 85% of the brain voxels and NAAG from a representative subject. Slice 5–16 were shown for the sake of visualization.

TABLE 2 | 2D and 3D intra-session CVs (%) for metabolites in different tissues and brain lobes (mean ± std).

		Glu	NAA	NAAG	tCho	tCr	Gly + Ins
2D	GM	3.30 ± 2.14	1.32 ± 0.83	2.60 ± 3.74	2.95 ± 1.64	2.75 ± 0.87	5.62 ± 1.46
	WM	3.34 ± 2.30	1.61 ± 1.09	3.94 ± 3.43	3.08 ± 1.88	2.63 ± 0.92	4.70 ± 3.58
	FRONTAL	3.49 ± 2.36	0.77 ± 0.11	3.55 ± 3.75	3.17 ± 3.69	4.07 ± 2.14	4.43 ± 1.04
	PARIETAL	5.88 ± 3.06	2.51 ± 2.23	1.68 ± 0.40	2.78 ± 1.17	2.69 ± 2.28	6.89 ± 2.49
3D	GM	0.30 ± 0.15	0.41 ± 0.01	2.76 ± 0.58	1.57 ± 1.45	0.60 ± 0.52	1.25 ± 0.25
	WM	0.52 ± 0.29	0.48 ± 0.37	1.20 ± 0.89	1.45 ± 1.39	0.73 ± 0.55	1.40 ± 0.99
	FRONTAL	0.61 ± 0.05	0.48 ± 0.41	2.67 ± 2.79	1.99 ± 1.02	0.76 ± 0.76	1.00 ± 1.09
	PARIETAL	0.63 ± 0.63	0.74 ± 0.35	1.82 ± 0.75	2.07 ± 2.06	0.74 ± 0.79	1.02 ± 1.05
	TEMPORAL	2.68 ± 1.27	1.29 ± 0.07	10.08 ± 6.42	2.23 ± 0.99	0.96 ± 0.69	2.87 ± 1.86
	OCCIPITAL	5.07 ± 1.57	0.97 ± 0.90	16.62 ± 1.44	2.43 ± 1.93	1.18 ± 0.83	3.77 ± 2.32

TR and TA. Whole-brain MRSI is usually applied without OVS to obtain metabolic information in the peripheral cortical regions. Such acquisition often relies on postprocessing strategies to suppress lipid signals such as data extrapolation (Haupt et al. 1996), L_2 regularization (Bilgic et al. 2014), Fast LIpid reconstruction and removal Processing (FLIP) (Adany et al. 2021), etc., with L_2 regularization being the most commonly applied approach. The L_2 regularization was directly applied to the dataset, however, it was challenging to find a regularization parameter that could effectively suppress lipid signals in the peripheral voxels without over-suppressing metabolite signals in the central voxels (Figure S1, Table S2). Note that with a regularization parameter that is optimal for the center voxels, residual lipids may remain in the peripheral voxels, potentially affecting metabolite quantification, particularly for NAA. Thus, we further optimized the L_2 regularization method to have different regularization parameters in different voxels, where the peripheral voxels tend to have higher regularizations (Figure 3). This is coherent with the intuition that the peripheral voxels have higher lipid contamination and thus need heavier regularizations. In addition to the L_2 and the adaptive voxel-wise L_2 regularization methods that were applied in the current study, the data extrapolation (Haupt et al. 1996) method and the FLIP (Adany et al. 2021) method might also be applied. However, these methods may require further adaptation, as their performance was

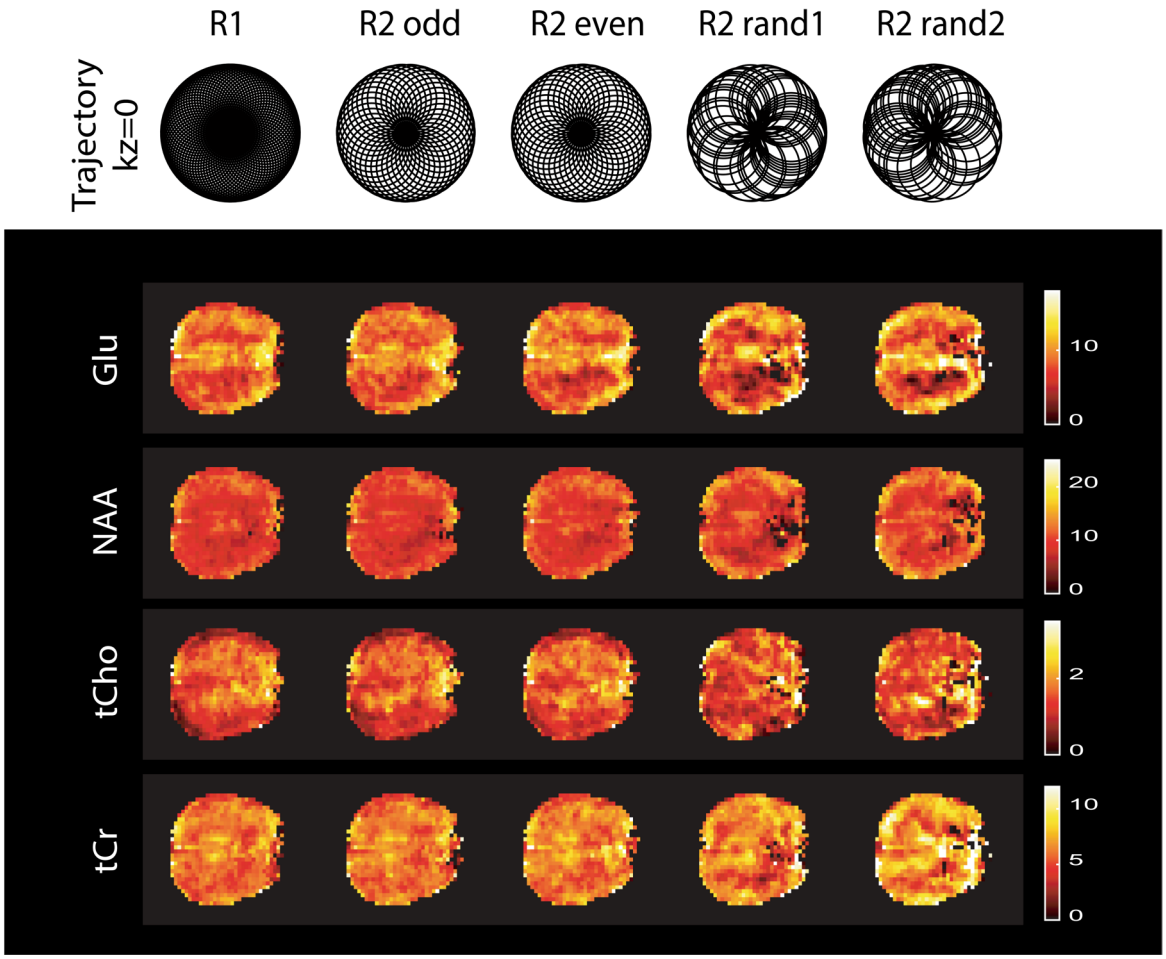

FIGURE 6 | Different undersampling schemes at R2: Row 1: K-space trajectories: The fully sampled trajectory R1, regularly undersampled trajectory R2 odd/even (every odd/even petal), randomly undersampled trajectory R2 rand1/rand2; row 2–5: Metabolic maps reconstructed from corresponding trajectories.

TABLE 3 | Incoherence metrics of undersampling schemes and their corresponding SSIM values for metabolic maps presented in Figure 6.

			SSIM				CRLB (75%)			
	ASPR	MSPR	Glu	tCr	NAA	tCho	Glu	tCr	NAA	tCho
R1	0.0006	0.3186	1	1	1	1	9	7	6	13
R2-even	0.0117	0.3530	0.91	0.91	0.87	0.92	11	7	6	15
R2-odd	0.0118	0.3497	0.91	0.91	0.85	0.91	11	7	6	16
R2-rand1	0.0154	0.3955	0.87	0.83	0.78	0.85	13	9	7	17
R2-rand2	0.0151	0.3790	0.87	0.85	0.8	0.88	13	8	6	17

optimized using data acquired with Cartesian trajectories at a TE of 16 ms or non-Cartesian trajectories at a TE of 50 ms. In those cases, lipid signals decayed around 3.3 or 50 times more than with the ultra-short TE of 0.83 ms/0.87 ms used in this study. Additionally, Cartesian trajectories typically offer better point spread functions and less lipid signal propagation compared to the non-Cartesian ones unless dedicatedly designed (Chiew et al. 2018; Hingerl et al. 2018; Steel et al. 2018).

We observed strong GM/WM contrasts in metabolic maps, with higher levels of tCho and NAAG in the WM, higher Glu levels in the GM, and uniform NAA in the GM and the WM. The spatial patterns of their concentrations were consistent with previous results (Klauser et al. 2021; Ziegs et al. 2023). For GSH and GABA, which were shown to be higher in the GM, no obvious contrasts were found. This can be due to their low concentrations and high spectral overlapping with high-signal-intensity metabolites (Mahmud et al. 2023; Ziegs et al. 2023). Dedicated methods such as MEGA (Peek et al. 2023) and SLOW (Weng et al. 2022) editing will be needed for robust quantification of these metabolites. Note that with a Hanning filter applied in the k-space, the effective voxel size is larger than the nominal voxel

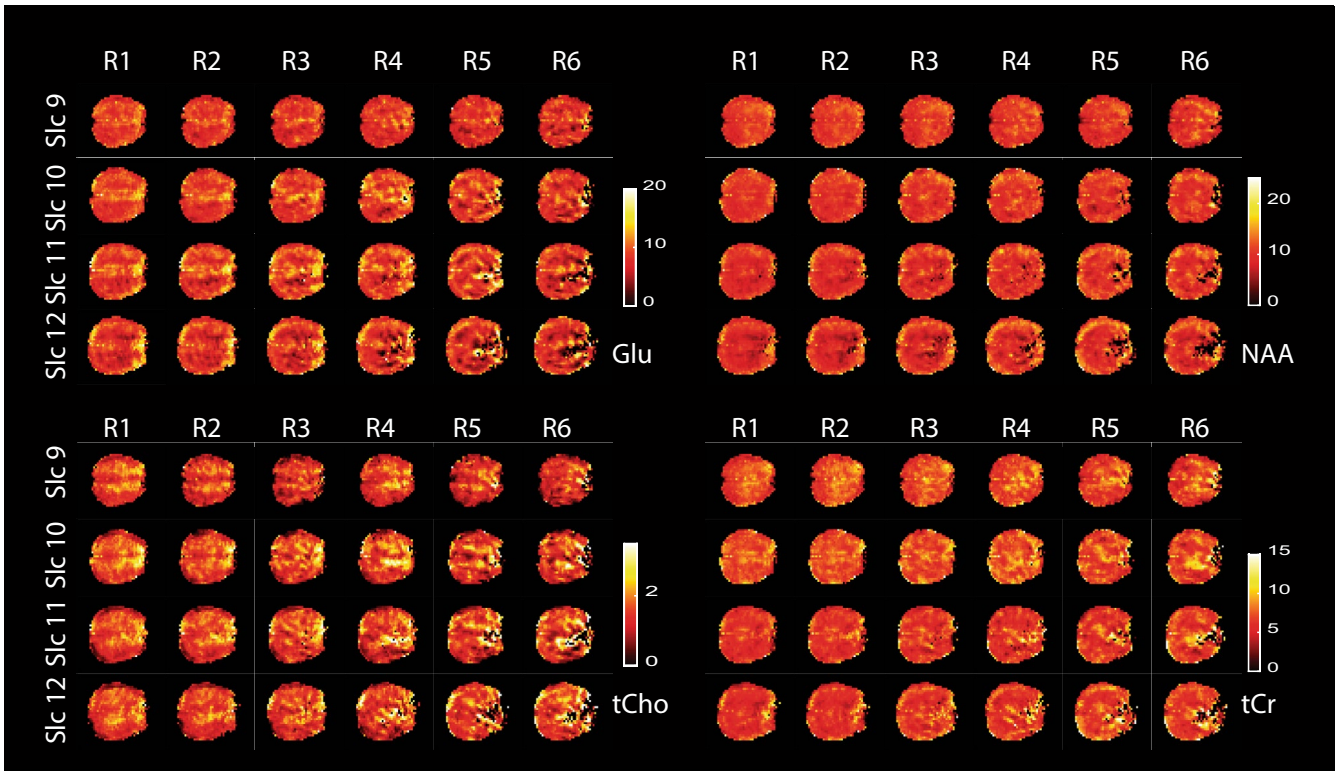

FIGURE 7 | 3D Glu, tCr, tCho, NAA metabolic maps (i.u) from the central four slices in a representative subject at different acceleration rates $R = 1, 2, 3, 4, 5, 6$.

size. Through SRF analysis (Figure S2), the effective voxel size is $6.23 \times 6.23\,mm^2$ for the 2D acquisition and $6.23 \times 6.23 \times 6.93\,mm^3$ for the 3D acquisition, which can give slightly blurrier maps compared with the nominal resolution of $4.48 \times 4.48\,mm^2$ and $4.48 \times 4.48 \times 4.50\,mm^3$.

The intra-session reproducibility can be influenced by subject motion and short-term scanner instability, such as frequency drift. The intra-session reproducibility of the 2D and 3D sequences was evaluated. Overall, the CVs of NAA, tCr, Gly + Ins, tCho, and Glu ranged from 0.2%–3.7%, 1.4%–5.5%, 0.5%–8.7%, 1.3%–9.7%, 0.1%–6.7% and 0.1%–2.6%, 0.3%–2.5%, 0.1%–6.8%, 0.1%–7.5%, 0.1%–5.6% for 2D and 3D respectively. Comparing CVs to previous studies is not straightforward due to differences in field strengths, quantification references, ROIs, scanning parameters, and limited studies reporting intra-session reproducibility. Using water as the quantification reference, whole-brain CVs of 13.73%, 19.86%, 15.10%, 31.13%, and 31.02% ($280 \times 280 \times 180\,mm^3$) and regional CVs of 2.8%–7.6%, 6.74%–8.53%, 4.24%–9.17%, 4.8%–10.3%, and 6.44%–12.08% (left/right frontal, parietal, occipital and temporal lobes) for NAA, tCho, tCr, Glx, and Ins were reported at 3T (EPSI, TA = 16 min) (Ding et al. 2015); using the peak height/peak area for quantification, whole brain CVs of 10.1%, 11.8%, 8.6% and 13.4%, 14.9%, 15.3% ($160 \times 160 \times 160\,mm^3$) were reported for NAA/Cr, Cho/Cr, and NAA/Cho respectively at 3T ((flyback) phase encoding CSI, TA = 7:48 min) (Bian et al. 2018); using tCr as the quantification reference, CVs of 9.3%, 6.9%, 6.5%, and 7.8% ($220 \times 220 \times 126\,mm^3$) were reported for Glx/tCr, tNAA/tCr, tCho/tCr, and Ins/tCr at 3T leveraging real-time motion correction (concentric rings, TA = 5:40 min) (Moser et al. 2020); Comparing the intra-session reproducibility with the inter-session reproducibility can be less straightforward, as intra-session CVs without repositioning the volunteers are expected to be lower than those of inter-session. However, there are also studies showing that the inter-session and intra-session reproducibilities are comparable (Hsu et al. 2001; Veenith et al. 2014). For inter-session reproducibility, at 7T, using water as an internal quantification reference, regional CVs of 3%–7%, 3%–6%, 4%–7%, 3%–5%, and 3%–7% (frontal, limbic, parietal, occipital, temporal) for NAA, tCr, Ins, tCho, and Glu in 3D data were reported (ECCENTRIC, TA = 6:16 min with low-rank reconstruction) (Klauser et al. 2023); using tCr as the quantification reference, regional CVs of 3%–8%, 2%–10%, 5%–13%, and 6%–16% (right/middle/left frontal/parietal lobes, phase-encoding CSI, TA = 30 min) and 7.0%, 5.9%, 7.0%, and 8.1% (GM/WM frontal, parietal, subcortical, phase-encoding CSI, TA = 5:11 min) for NAA/tCr, tCho/tCr, Ins/tCr, and Glu/tCr were reported respectively (Bogner et al. 2012; Heckova et al. 2020). At 9.4 T, CVs reported range from 6.2%–8.5%, 4.6%–5.1%, 6.5%–10.3%, and 7.4%–16.7% ($220 \times 220 \times 80\,mm^3$) for NAA/tCr, tCho/tCr, Glu/tCr, and Ins/tCr (phase-encoding CSI, TA = 10 min) (Ziegs et al. 2023). The present CV values were similar but slightly lower than those reported in these studies. The CVs were, in general, higher in the frontal lobe, which can be attributed to the higher B_0 field inhomogeneity since the frontal lobe is close to the air-filled sinuses. Higher-order shims and a local shim coil can be incorporated into future experimental setups to improve B_0 field inhomogeneity, especially at the frontal lobe, by static and dynamic shimming (Boer et al. 2022; Kumaragamage et al. 2024). Except for the SNR and B_0 inhomogeneity, the reproducibility can also be influenced by B_1^+ inhomogeneities and subject motions. The acquired B_1^+ maps could be included in the correction of metabolite quantification, and incorporating self-guided frequency and phase correction in

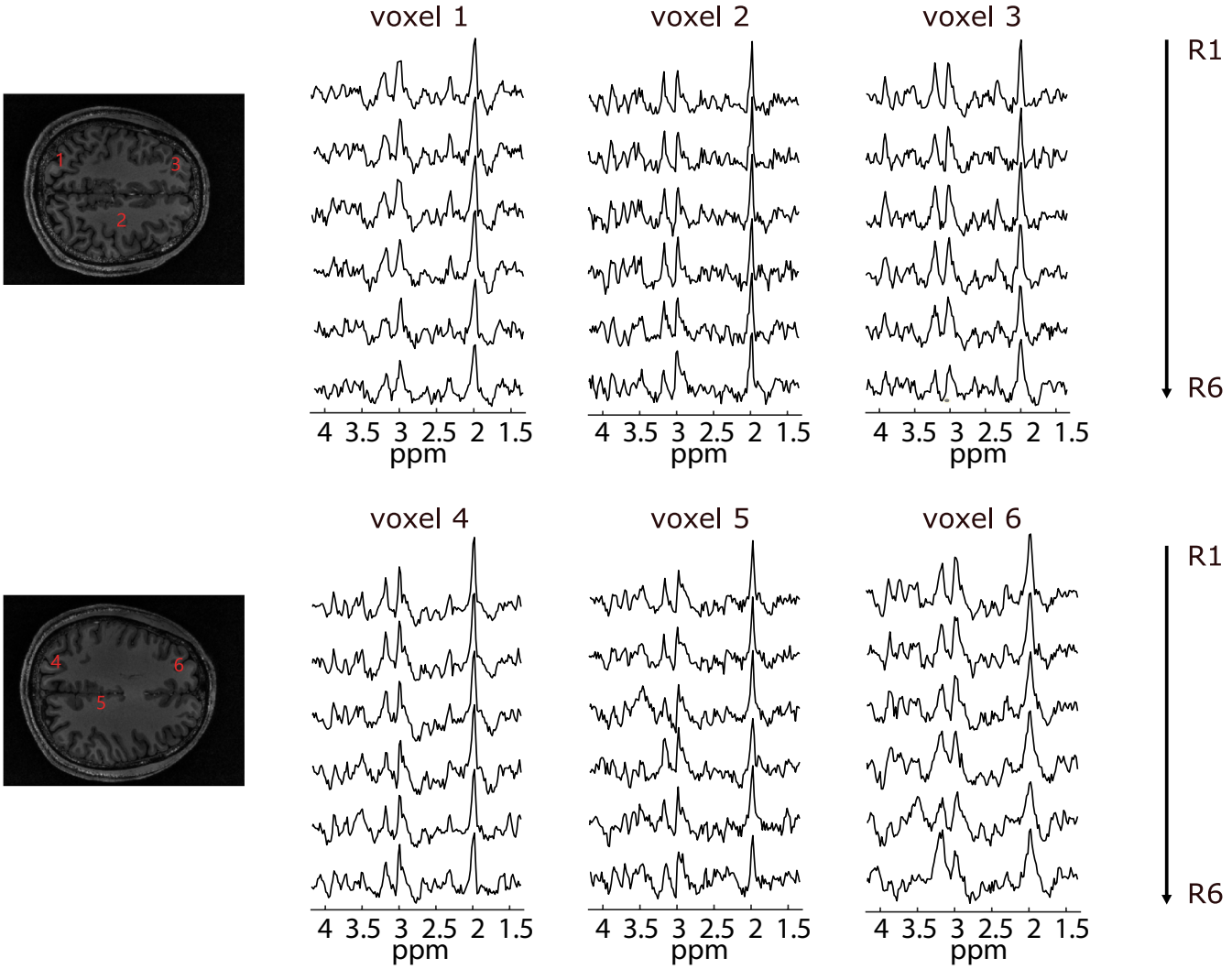

FIGURE 8 | Representative spectra from six different voxels in two different slices from a representative subject at acceleration rates $R = 1, 2, 3, 4, 5, 6$.

the future could reduce the influence of motions. Additionally, through correlation analysis of metabolite CVs and CRLBs, a significant positive correlation was found with NAAG, for which the quantification is more challenging due to the low concentration and spectral overlapping (Figure S3, Table S3).

We explored the possibilities of combining RSI with CS. It was shown that for 3D data, the SSIM index remained above 0.85 and 0.80 for Glu, NAA, tCr, and tCho for all subjects until $R = 2$ and $R = 3$, corresponding to an acquisition time of 2:19 min and 1:52 min, respectively. It was noted that different metabolites might have different maximum acceleration rates (Bogner et al. 2014). For example, the SSIM for Glu, NAA, tCr, and tCho were above 0.8 until $R = 3$, while until $R = 2$ for Gly + Ins. Furthermore, with the increase of acceleration rates, the metabolite concentrations decreased. This might be related to the degradation in SNR with a higher acceleration factor, leading to bias in metabolite quantification (Bartha 2007; Zöllner et al. 2020). Note that petals were undersampled uniformly, that is, every R petal was sampled. This is because the rosette trajectory was designed based on the stochastic trajectory (Noll 1997), which is intrinsically incoherent. Furthermore, lipid signals are orders of magnitude larger than the metabolite signals. MRSI without lipid pre-saturation can suffer from aliased lipid signals at higher acceleration rates, as they can propagate inside the brain and interfere with the metabolite signals (Figure S4), limiting the performance of CS. In this work, parallel imaging combined with CS (Uecker et al. 2013) was implemented to improve the metabolite SNR (Nassirpour, Chang, Avdievitch, and Henning 2018), achieving an acceleration rate of 2–3. Higher acceleration rates might be achieved by removing the lipid signals before reconstruction (Klauser et al. 2019, 2021). Noteworthily, as proof of concept, the BART package and the total variation regularization were used for CS, with the same regularization parameter applied for different acceleration rates. However, total variation regularization can lead to smooth reconstructions and potential staircase artifacts that can blur brain structures (Block et al. 2007). By applying or combining different regularization terms such as total generalized variation (TGV), wavelet regularization, etc., artifacts caused by the acceleration might be better alleviated and overall image quality can be improved. Additionally, applying CS along both the spatial and the temporal dimensions can better leverage the spatial-spectral sparsity property of

TABLE 4 | Metabolite concentrations (i.u), third-quartile CRLBs, and SSIM at different acceleration rates (mean ± std).

		R1	R2	R3	R4	R5	R6
SSIM	Glu	1.00 ± 0.00	0.89 ± 0.05	0.84 ± 0.04	0.81 ± 0.05	0.77 ± 0.04	0.76 ± 0.04
	NAA	1.00 ± 0.00	0.89 ± 0.04	0.85 ± 0.05	0.81 ± 0.06	0.78 ± 0.05	0.77 ± 0.06
	tCho	1.00 ± 0.00	0.87 ± 0.03	0.82 ± 0.02	0.79 ± 0.03	0.76 ± 0.02	0.73 ± 0.02
	tCr	1.00 ± 0.00	0.89 ± 0.05	0.85 ± 0.04	0.81 ± 0.05	0.79 ± 0.04	0.76 ± 0.04
	Gly + Ins	1.00 ± 0.00	0.84 ± 0.05	0.78 ± 0.03	0.76 ± 0.04	0.75 ± 0.04	0.72 ± 0.03
Conc (i.u)	Glu	8.29 ± 1.63	7.90 ± 1.75	7.38 ± 1.95	7.09 ± 2.04	6.54 ± 2.20	6.48 ± 1.84
	NAA	10.56 ± 0.66	10.41 ± 0.89	10.46 ± 0.88	10.62 ± 0.91	9.78 ± 1.37	9.54 ± 1.52
	tCho	1.95 ± 0.48	1.87 ± 0.52	1.77 ± 0.44	1.72 ± 0.39	1.63 ± 0.35	1.58 ± 0.40
	tCr	7.54 ± 0.51	7.51 ± 0.40	7.15 ± 0.31	7.03 ± 0.50	6.56 ± 0.77	6.45 ± 0.89
	Gly + Ins	3.97 ± 1.01	3.75 ± 0.98	3.48 ± 0.87	3.43 ± 0.90	3.56 ± 0.85	3.47 ± 0.86
CRLB	Glu	12.08 ± 2.74	13.33 ± 2.52	14.00 ± 3.00	14.33 ± 2.89	16.67 ± 4.04	17.33 ± 3.79
	NAA	8.33 ± 2.31	8.33 ± 2.31	8.00 ± 1.73	8.33 ± 1.53	9.00 ± 1.73	9.67 ± 2.08
	tCho	11.67 ± 2.08	13.33 ± 2.52	14.67 ± 2.52	15.67 ± 3.06	16.00 ± 1.73	18.67 ± 4.73
	tCr	8.33 ± 0.58	8.67 ± 0.58	9.00 ± 1.00	9.33 ± 1.53	10.33 ± 1.53	11.00 ± 2.00
	Gly + Ins	18.00 ± 5.20	18.33 ± 3.51	20.00 ± 1.73	21.00 ± 1.00	21.33 ± 2.08	23.00 ± 2.65

MRSI datasets, and thus potentially gives improved reconstruction quality. For example, Nassirpour et al. have applied 3D TV regularizations (2 spatial dimensions + time dimension) combined with a 2D wavelet regularization (2 spatial dimensions) in undersampled non-lipid-suppressed cartesian MRSI datasets to balance the potential smoothing effect of TV and patchiness artifacts of wavelet regularizations (Nassirpour, Chang, and Henning 2018) and have achieved acceleration rates of 4–5. They also showed that with low-rank reconstruction, there would be fewer lipid artifacts compared with pure CS reconstruction. Klauser et al. have applied the low-rank model with TGV in both Cartesian and non-Cartesian MRSI datasets (Klauser et al. 2021, 2023), achieving acceleration factors of 2–4 with minimal acceleration distortion. Except for the conventional methods, machine learning based techniques can also be exploited for undersampled MRSI reconstruction (Nassirpour, Chang, and Henning 2018).

The rosette trajectory (in our case $\omega_1 = \omega_2$) provides a gradient-friendly method for MRSI due to its smooth sinusoidal gradient waveform. This is favorable as it mitigates gradient system and physiological (PNS) limitations and enables high spectral bandwidth and spatial resolution, particularly at ultra-high fields. Characteristically, each petal of the rosette crosses the k-space center, enabling self-guided correction techniques for frequency drifts and motions (Senthil et al. 2023). This makes RSI more robust to systematic frequency drift and motions. Additionally, its inherently incoherent sampling pattern makes it more compatible with CS. There are less favorable characteristics. Compared to EPSI, RSI oversamples the k-space center (Figure S5d,e), improving the SNR, but the non-uniform sampling comes with lower sampling efficiency (Schirda et al. 2009). Compared with other common non-uniform trajectories (Figure S5a–d), RSI samples the outer k-space denser, potentially broadening the SRF and influencing the SNR efficiency. Earlier studies have shown that a sampling density approaching a Hanning filter improves SRF and SNR (Greiser and von Kienlin, 2003; Mareci and Brooker, 1991). Several studies have focused on improving the SRF and/or SNR of metabolic imaging by finding new trajectories with a more favorable sampling density. For example, the egg-shaped modified rosette trajectory was proposed where the temporal SNR was reported to have increased by up to 12% compared to the conventional rosette (Blömer et al. 2024); density-weighted concentric ring trajectories were proposed to improve the SRF with reduced side lobes and to elevate SNR (Chiew et al. 2018; Hingerl et al. 2018; Steel et al. 2018); density-weighted spiral trajectory was proposed to reduce ringing artifacts with comparable SNR as the standard spiral trajectory (Adalsteinsson et al. 1999). In addition, smooth gradient transitions and potential redundant sampling in some regions result in slower k-space traversal. In this study, we combined the rosette trajectory with CS by exploiting its inherent incoherent k-space sampling to explore the potential of further reducing the acquisition time.

This study has several limitations. First, compared with conventional CSI, fast trajectories are more prone to some undesirable effects such as eddy currents, gradient imperfections, and B_0 field inhomogeneity. These effects can cause a deviation of the actual trajectory from the designed trajectory, leading to a worse point spread function and thus broader linewidth. To further improve the spectral quality, B_0 field correction can be included. Besides, fast-changing gradients can induce a high-frequency drift rate (Windschuh et al. 2019) due to gradient heating, thus leading to broader linewidth. The rosette trajectory, passing the k-space center in each TR, allows for self-correction of the frequency drift and motion artifacts. To

further improve the spectral quality (linewidth, SNR) and reproducibility, frequency drift, and motion correction will be included in the next step (Senthil et al. 2023). Third, macromolecule signals are pronounced at ultra-short TE, which can bias metabolite quantification (Cudalbu et al. 2021; Schaller et al. 2013). Here, the macromolecule basis was simulated within LCModel (Provencher 2001; Schaller et al. 2013). Compared with a measured in vivo macromolecule spectrum, using a simulated basis can lead to less precision and lower reproducibility due to inadequate characterization of the MM spectrum (Birch et al. 2017; Heckova et al. 2020). To further improve the quantification accuracy and reproducibility, the MM spectrum can be measured and incorporated in the basis set.

5 | Conclusion

2D and 3D whole-brain slab metabolic maps of major ^{1}H metabolites such as NAA, Glu, tCr, tCho, and Gly + Ins were achieved using the non-lipid-suppressed ultra-short-TE-FID RSI with improved water suppression performance at 7T. It took 21.33 s to acquire a one-average 2D slice with a resolution of $4.48 \times 4.48\,mm^2$ and 5:38 min to acquire 3D metabolic maps with a nominal resolution of $4.48 \times 4.48 \times 4.50\,mm^3$. With CS, the 3D acquisition can be further reduced to around 2 min. The current implementation of ^{1}H-FID-RSI allows for a fast and reproducible measurement of the spatial metabolic distribution in the human brain, thereby paving the way for a better understanding of brain functions and pathology.

Acknowledgements

This work is supported by Swiss National Science Foundation NO.: 189064, 213769. We acknowledge the MRI Platform of the FCBG (Fondation Campus Biotech Geneva) and the CIBM Center for Biomedical Imaging for providing expertise and resources to conduct this study.

Ethics Statement

The study was approved by Swiss cantonal ethics committee. All volunteers gave informed consent in accordance with the ethics before the experiments.

Conflicts of Interest

The authors state that they have no known financial conflicts of interest or personal relationships that could have influenced the work presented in this paper.

Data Availability Statement

The data that support the findings of this study are available upon request from the corresponding author. The data are not publicly available due to privacy and ethical restrictions related to the study subjects.

References

Adany, P., I.-Y. Choi, and P. Lee. 2021. "Method for Fast Lipid Reconstruction and Removal Processing in 1H MRSI of the Brain." *Magnetic Resonance in Medicine* 86, no. 6: 2930–2944. https://doi.org/10.1002/mrm.28949.

Bartha, R. 2007. "Effect of Signal-to-Noise Ratio and Spectral Linewidth on Metabolite Quantification at 4 T." *NMR in Biomedicine* 20, no. 5: 512–521. https://doi.org/10.1002/nbm.1122.

Bian, W., Y. Li, J. C. Crane, and S. J. Nelson. 2018. "Fully Automated Atlas-Based Method for Prescribing 3D PRESS MR Spectroscopic Imaging: Toward Robust and Reproducible Metabolite Measurements in Human Brain." *Magnetic Resonance in Medicine* 79, no. 2: 636–642. https://doi.org/10.1002/mrm.26718.

Bilgic, B., I. Chatnuntawech, A. P. Fan, et al. 2014. "Fast Image Reconstruction With L2-Regularization." *Journal of Magnetic Resonance Imaging: JMRI* 40, no. 1: 181–191. https://doi.org/10.1002/jmri.24365.

Birch, R., A. C. Peet, H. Dehghani, and M. Wilson. 2017. "Influence of Macromolecule Baseline on 1H MR Spectroscopic Imaging Reproducibility." *Magnetic Resonance in Medicine* 77, no. 1: 34–43. https://doi.org/10.1002/mrm.26103.

Blömer, S., L. Hingerl, M. Marjańska, et al. 2024. "Proton-Free Induction Decay MRSI at 7 T in the Human Brain Using an Egg-Shaped Modified Rosette K-Space Trajectory." *Magnetic Resonance in Medicine* 93, no. 4: 43–57. https://doi.org/10.1002/mrm.30368.

Bluestein, K. T., D. Pitt, M. V. Knopp, and P. Schmalbrock. 2012. "T1 and Proton Density at 7 T in Patients With Multiple Sclerosis: An Initial Study." *Magnetic Resonance Imaging* 30, no. 1: 19–25. https://doi.org/10.1016/j.mri.2011.07.018.

Boer, V. O., J. O. Pedersen, N. Arango, I. Kuang, J. Stockmann, and E. T. Petersen. 2022. "Improving Brain B0 Shimming Using an Easy and Accessible Multi-Coil Shim Array at Ultra-High Field." *Magnetic Resonance Materials in Physics, Biology and Medicine* 35, no. 6: 943–951. https://doi.org/10.1007/s10334-022-01014-6.

Bogner, W., A. T. Hess, B. Gagoski, et al. 2014. "Real-Time Motion- and B0-Correction for LASER-Localized Spiral-Accelerated 3D-MRSI of the Brain at 3T." *NeuroImage* 88: 22–31. https://doi.org/10.1016/j.neuroimage.2013.09.034.

Bogner, W., R. Otazo, and A. Henning. 2021. "Accelerated MR Spectroscopic Imaging—A Review of Current and Emerging Techniques." *NMR in Biomedicine* 34, no. 5: e4314. https://doi.org/10.1002/nbm.4314.

Bogner, W., S. Gruber, S. Trattnig, and M. Chmelik. 2012. "High-Resolution Mapping of Human Brain Metabolites by Free Induction Decay 1H MRSI at 7 T." *NMR in Biomedicine* 25, no. 6: 873–882. https://doi.org/10.1002/nbm.1805.

Breuer, F. A., M. Blaimer, M. F. Mueller, et al. 2006. "Controlled Aliasing in Volumetric Parallel Imaging (2D CAIPIRINHA)." *Magnetic Resonance in Medicine* 55, no. 3: 549–556. https://doi.org/10.1002/mrm.20787.

Bucholz, E. K., J. Song, G. A. Johnson, and I. Hancu. 2008. "Multispectral Imaging With Three-Dimensional Rosette Trajectories." *Magnetic Resonance in Medicine* 59, no. 3: 581–589. https://doi.org/10.1002/mrm.21551.

Chiew, M., W. Jiang, B. Burns, et al. 2018. "Density-Weighted Concentric Rings k-Space Trajectory for 1 H Magnetic Resonance Spectroscopic Imaging at 7 T." *NMR in Biomedicine* 31, no. 1: e3838. https://doi.org/10.1002/nbm.3838.

Collins, D. L., C. J. Holmes, T. M. Peters, and A. C. Evans. 1995. "Automatic 3-D Model-Based Neuroanatomical Segmentation." *Human Brain Mapping* 3, no. 3: 190–208. https://doi.org/10.1002/hbm.460030304.

Cudalbu, C., K. L. Behar, P. K. Bhattacharyya, et al. 2021. "Contribution of Macromolecules to Brain 1 H MR Spectra: Experts' Consensus Recommendations." *NMR in Biomedicine* 34, no. 5: e4393. https://doi.org/10.1002/nbm.4393.

Deshmane, A., V. Gulani, M. A. Griswold, and N. Seiberlich. 2012. "Parallel MR Imaging." *Journal of Magnetic Resonance Imaging: JMRI* 36, no. 1: 55–72. https://doi.org/10.1002/jmri.23639.

Ding, X.-Q., A. A. Maudsley, M. Sabati, S. Sheriff, P. R. Dellani, and H. Lanfermann. 2015. "Reproducibility and Reliability of Short-TE Whole-Brain MR Spectroscopic Imaging of Human Brain at 3T." *Magnetic Resonance in Medicine* 73, no. 3: 921–928. https://doi.org/10.1002/mrm.25208.

Fessler, J. A., and B. P. Sutton. 2003. "Nonuniform Fast Fourier Transforms Using Min-Max Interpolation." *IEEE Transactions on Signal Processing* 51, no. 2: 560–574. https://doi.org/10.1109/TSP.2002.807005.

Gagoski, B. A. 2011. *Magnetic Resonance Spectroscopic Imaging Using Parallel Transmission at 7T*. Massachusetts Institute of Technology. https://dspace.mit.edu/handle/1721.1/63069.

Govindaraju, V., K. Young, and A. A. Maudsley. 2000. "Proton NMR Chemical Shifts and Coupling Constants for Brain Metabolites." *NMR in Biomedicine* 13, no. 3: 129–153. https://doi.org/10.1002/1099-1492(200005)13:3<129::AID-NBM619>3.0.CO;2-V.

Griswold, M. A., P. M. Jakob, R. M. Heidemann, et al. 2002. "Generalized Autocalibrating Partially Parallel Acquisitions (GRAPPA)." *Magnetic Resonance in Medicine* 47, no. 6: 1202–1210. https://doi.org/10.1002/mrm.10171.

Hangel, G., B. Strasser, M. Považan, et al. 2018. "Ultra-High Resolution Brain Metabolite Mapping at 7 T by Short-TR Hadamard-Encoded FID-MRSI." *NeuroImage* 168: 199–210. https://doi.org/10.1016/j.neuroimage.2016.10.043.

Haupt, C. I., N. Schuff, M. W. Weiner, and A. A. Maudsley. 1996. "Removal of Lipid Artifacts in 1H Spectroscopic Imaging by Data Extrapolation." *Magnetic Resonance in Medicine* 35, no. 5: 678–687. https://doi.org/10.1002/mrm.1910350509.

Heckova, E., M. Považan, B. Strasser, et al. 2020. "Effects of Different Macromolecular Models on Reproducibility of FID-MRSI at 7T." *Magnetic Resonance in Medicine* 83, no. 1: 12–21. https://doi.org/10.1002/mrm.27922.

Hiba, B., B. Faure, L. Lamalle, M. Décorps, and A. Ziegler. 2003. "Out-and-In Spiral Spectroscopic Imaging in Rat Brain at 7 T." *Magnetic Resonance in Medicine* 50, no. 6: 1127–1133. https://doi.org/10.1002/mrm.10622.

Hingerl, L., W. Bogner, P. Moser, et al. 2018. "Density-Weighted Concentric Circle Trajectories for High Resolution Brain Magnetic Resonance Spectroscopic Imaging at 7T." *Magnetic Resonance in Medicine* 79, no. 6: 2874–2885. https://doi.org/10.1002/mrm.26987.

Hsu, Y. Y., M. C. Chen, K. E. Lim, and C. Chang. 2001. "Reproducibility of Hippocampal Single-Voxel Proton MR Spectroscopy and Chemical Shift Imaging." *AJR. American Journal of Roentgenology* 176, no. 2: 529–536. https://doi.org/10.2214/ajr.176.2.1760529.

Jenkinson, M., C. F. Beckmann, T. E. J. Behrens, M. W. Woolrich, and S. M. Smith. 2012. "FSL." *NeuroImage* 62, no. 2: 782–790. https://doi.org/10.1016/j.neuroimage.2011.09.015.

Klauser, A., B. Strasser, B. Thapa, F. Lazeyras, and O. Andronesi. 2021. "Achieving High-Resolution 1H-MRSI of the Human Brain With Compressed-Sensing and Low-Rank Reconstruction at 7 Tesla." *Journal of Magnetic Resonance* 331: 107048. https://doi.org/10.1016/j.jmr.2021.107048.

Klauser, A., B. Strasser, W. Bogner, et al. 2023. "ECCENTRIC: A Fast and Unrestrained Approach for High-Resolution In Vivo Metabolic Imaging at Ultra-High Field MR. *ArXiv*, arXiv:2305.13822v1".

Klauser, A., S. Courvoisier, J. Kasten, et al. 2019. "Fast High-Resolution Brain Metabolite Mapping on a Clinical 3T MRI by Accelerated H-FID-MRSI and Low-Rank Constrained Reconstruction." *Magnetic Resonance in Medicine* 81, no. 5: 2841–2857. https://doi.org/10.1002/mrm.27623.

Kumaragamage, C., S. McIntyre, T. W. Nixon, H. M. De Feyter, and R. A. de Graaf. 2024. "High-Quality Lipid Suppression and B0 Shimming for Human Brain 1H MRSI." *NeuroImage* 300: 120845. https://doi.org/10.1016/j.neuroimage.2024.120845.

Landheer, K., and C. Juchem. 2019. "Dephasing Optimization Through Coherence Order Pathway Selection (DOTCOPS) for Improved Crusher Schemes in MR Spectroscopy." *Magnetic Resonance in Medicine* 81, no. 4: 2209–2222. https://doi.org/10.1002/mrm.27587.

Lin, L., M. Považan, A. Berrington, Z. Chen, and P. B. Barker. 2019. "Water Removal in MR Spectroscopic Imaging With L2 Regularization." *Magnetic Resonance in Medicine* 82, no. 4: 1278–1287. https://doi.org/10.1002/mrm.27824.

Lustig, M., D. Donoho, and J. M. Pauly. 2007. "Sparse MRI: The Application of Compressed Sensing for Rapid MR Imaging." *Magnetic Resonance in Medicine* 58, no. 6: 1182–1195. https://doi.org/10.1002/mrm.21391.

Mahmud, S. Z., T. S. Denney, and A. Bashir. 2023. "High-Resolution Proton Metabolic Mapping of the Human Brain at 7 T Using Free Induction Decay Rosette Spectroscopic Imaging." *NMR in Biomedicine* 37, no. 1: e5042. https://doi.org/10.1002/nbm.5042.

Marques, J. P., T. Kober, G. Krueger, W. van der Zwaag, P.-F. Van de Moortele, and R. Gruetter. 2010. "MP2RAGE, a Self Bias-Field Corrected Sequence for Improved Segmentation and T1-Mapping at High Field." *NeuroImage* 49, no. 2: 1271–1281. https://doi.org/10.1016/j.neuroimage.2009.10.002.

Mazziotta, J., A. Toga, A. Evans, et al. 2001. "A Probabilistic Atlas and Reference System for the Human Brain: International Consortium for Brain Mapping (ICBM)." *Philosophical Transactions of the Royal Society of London, Series B* 356, no. 1412: 1293–1322. https://doi.org/10.1098/rstb.2001.0915.

Moser, P., K. Eckstein, L. Hingerl, et al. 2020. "Intra-Session and Inter-Subject Variability of 3D-FID-MRSI Using Single-Echo Volumetric EPI Navigators at 3T." *Magnetic Resonance in Medicine* 83, no. 6: 1920–1929. https://doi.org/10.1002/mrm.28076.

Mulkern, R. V., and L. P. Panych. 2001. "Echo Planar Spectroscopic Imaging." *Concepts in Magnetic Resonance* 13, no. 4: 213–237. https://doi.org/10.1002/cmr.1011.

Nassirpour, S., P. Chang, and A. Henning. 2018. "High and Ultra-High Resolution Metabolite Mapping of the Human Brain Using 1H FID MRSI at 9.4T." *NeuroImage* 168: 211–221. https://doi.org/10.1016/j.neuroimage.2016.12.065.

Nassirpour, S., P. Chang, N. Avdievitch, and A. Henning. 2018. "Compressed Sensing for High-Resolution Nonlipid Suppressed 1H FID MRSI of the Human Brain at 9.4T." *Magnetic Resonance in Medicine* 80, no. 6: 2311–2325. https://doi.org/10.1002/mrm.27225.

Noll, D. C. 1997. "Multishot Rosette Trajectories for Spectrally Selective MR Imaging." *IEEE Transactions on Medical Imaging* 16, no. 4: 372–377. https://doi.org/10.1109/42.611345.

Ogg, R. J., P. B. Kingsley, and J. S. Taylor. 1994. "WET, a T1- and B1-Insensitive Water-Suppression Method for In Vivo Localized 1H NMR Spectroscopy." *Journal of Magnetic Resonance. Series B* 104, no. 1: 1–10. https://doi.org/10.1006/jmrb.1994.1048.

Ozdemir, M. S., Y. De Deene, Y. D'Asseler, and I. Lemahieu. 2006. "Removal of Sideband Modulations in 1H-MRS Without Solvent Suppression." In *International Society for Magnetic Resonance in Medicine (ISMRM) 14th Scientific Meeting, Proceedings*, S18–24. International Society for Magnetic Resonance in Medicine.

Peek, A. L., T. J. Rebbeck, A. M. Leaver, et al. 2023. "A Comprehensive Guide to MEGA-PRESS for GABA Measurement." *Analytical Biochemistry* 669: 115113. https://doi.org/10.1016/j.ab.2023.115113.

Provencher, S. W. 2001. "Automatic Quantitation of Localized In Vivo 1H Spectra With LCModel." *NMR in Biomedicine* 14, no. 4: 260–264. https://doi.org/10.1002/nbm.698.

Pruessmann, K. P., M. Weiger, M. B. Scheidegger, and P. Boesiger. 1999. "SENSE: Sensitivity Encoding for Fast MRI." *Magnetic Resonance in Medicine* 42, no. 5: 952–962. https://doi.org/10.1002/(SICI)1522-2594(199911)42:5<952::AID-MRM16>3.0.CO;2-S.

Schaller, B., L. Xin, C. Cudalbu, and R. Gruetter. 2013. "Quantification of the Neurochemical Profile Using Simulated Macromolecule Resonances at 3T." *NMR in Biomedicine* 26, no. 5: 593–599. https://doi.org/10.1002/nbm.2896.

Schirda, C. V., C. Tanase, and F. E. Boada. 2009. "Rosette Spectroscopic Imaging: Optimal Parameters for Alias-Free, High Sensitivity Spectroscopic Imaging." *Journal of Magnetic Resonance Imaging: JMRI* 29, no. 6: 1375–1385. https://doi.org/10.1002/jmri.21760.

Schirda, C. V., T. Zhao, O. C. Andronesi, et al. 2016. "In Vivo Brain Rosette Spectroscopic Imaging (RSI) With LASER Excitation, Constant Gradient Strength Readout, and Automated LCModel Quantification for all Voxels: In Vivo Brain 3D LASER-RSI." *Magnetic Resonance in Medicine* 76, no. 2: 380–390. https://doi.org/10.1002/mrm.25896.

Senthil, S., B. Kadota, P. Truong, and J. Near. 2023. "Retrospective Frequency Drift Correction of Rosette MRSI Data Using Spectral Registration." *Magnetic Resonance in Medicine* 90, no. 4: 1271–1281. https://doi.org/10.1002/mrm.29760.

Serrai, H., D. B. Clayton, L. Senhadji, C. Zuo, and R. E. Lenkinski. 2002. "Localized Proton Spectroscopy Without Water Suppression: Removal of Gradient Induced Frequency Modulations by Modulus Signal Selection." *Journal of Magnetic Resonance* 154, no. 1: 53–59. https://doi.org/10.1006/jmre.2001.2462.

Steel, A., M. Chiew, P. Jezzard, et al. 2018. "Metabolite-Cycled Density-Weighted Concentric Rings k-Space Trajectory (DW-CRT) Enables High-Resolution 1 H Magnetic Resonance Spectroscopic Imaging at 3-Tesla." *Scientific Reports* 8, no. 1: 7792. https://doi.org/10.1038/s41598-018-26096-y.

Tkáč, I., D. Deelchand, W. Dreher, et al. 2021. "Water and Lipid Suppression Techniques for Advanced 1H MRS and MRSI of the Human Brain: Experts' Consensus Recommendations." *NMR in Biomedicine* 34, no. 5: e4459. https://doi.org/10.1002/nbm.4459.

Uecker, M., P. Lai, M. J. Murphy, et al. 2014. "ESPIRiT—An Eigenvalue Approach to Autocalibrating Parallel MRI: Where SENSE Meets GRAPPA." *Magnetic Resonance in Medicine* 71, no. 3: 990–1001. https://doi.org/10.1002/mrm.24751.

Uecker, M., P. Virtue, F. Ong, et al. 2013. "Software Toolbox and Programming Library for Compressed Sensing and Parallel Imaging." In *ISMRM Scientific Workshop - Data Sampling and Image Reconstruction, Sedona, Arizona, USA, 2013. Abstract number: Section 8, Number 6*. International society for magnetic resonance in medicine.

Veenith, T. V., M. Mada, E. Carter, et al. 2014. "Comparison of Inter Subject Variability and Reproducibility of Whole Brain Proton Spectroscopy." *PLoS One* 9, no. 12: e115304. https://doi.org/10.1371/journal.pone.0115304.

Walsh, D. O., A. F. Gmitro, and M. W. Marcellin. 2000. "Adaptive Reconstruction of Phased Array MR Imagery." *Magnetic Resonance in Medicine* 43, no. 5: 682–690. https://doi.org/10.1002/(SICI)1522-2594(200005)43:5<682::AID-MRM10>3.0.CO;2-G.

Wei, E., and A. Ozdaglar. 2012. "Distributed Alternating Direction Method of Multipliers." In *2012 IEEE 51st IEEE Conference on Decision and Control (CDC)*, 5445–5450. Institute of Electrical and Electronics Engineers (IEEE).

Weng, G., P. Radojewski, S. Sheriff, et al. 2022. "SLOW: A Novel Spectral Editing Method for Whole-Brain MRSI at Ultra High Magnetic Field." *Magnetic Resonance in Medicine* 88, no. 1: 53–70. https://doi.org/10.1002/mrm.29220.

Windschuh, J., M. Zaiss, P. Ehses, J.-S. Lee, A. Jerschow, and R. R. Regatte. 2019. "Assessment of Frequency Drift on CEST MRI and Dynamic Correction: Application to gagCEST at 7T." *Magnetic Resonance in Medicine* 81, no. 1: 573–582. https://doi.org/10.1002/mrm.27367.

Xin, L., B. Schaller, V. Mlynarik, H. Lu, and R. Gruetter. 2013. "Proton T1 Relaxation Times of Metabolites in Human Occipital White and Gray Matter at 7 T." *Magnetic Resonance in Medicine* 69, no. 4: 931–936. https://doi.org/10.1002/mrm.24352.

Ziegs, T., A. M. Wright, and A. Henning. 2023. "Test–Retest Reproducibility of Human Brain Multi-Slice H FID-MRSI Data at 9.4T After Optimization of Lipid Regularization, Macromolecular Model, and Spline Baseline Stiffness." *Magnetic Resonance in Medicine* 89, no. 1: 11–28. https://doi.org/10.1002/mrm.29423.

Zöllner, H. J., M. Považan, S. C. N. Hui, S. Tapper, R. A. E. Edden, and G. Oeltzschner. 2020. "Comparison of Algorithms for Linear-Combination Modelling of Short-Echo-Time Magnetic Resonance Spectra (p. 2020.06.05.136796). bioRxiv." https://doi.org/10.1101/2020.06.05.136796.

Supporting Information

Additional supporting information can be found online in the Supporting Information section.